A New Model for the Equilibrium Shape of Raindrops

KENNETH V. BEARD* AND CATHERINE CHUANG*

Department of Atmospheric Sciences, University of Illinois at Urbana-Champaign, IL 61801

(Manuscript received 21 April 1986, in final form 4 December 1986)

ABSTRACT

The equilibrium shape of raindrops has been determined from Laplace's equation using an internal hydrostatic pressure with an external aerodynamic pressure based on measurements for a sphere but adjusted for the effect of distortion. The drop shape was calculated by integration from the upper pole with the initial curvature determined by iteration on the drop volume. The shape was closed at the lower pole by adjusting either the pressure drag or the drop weight to achieve an overall force balance. Model results provide bounds on the axis ratio of raindrops with an uncertainty of about 1% and very good agreement with extensive wind tunnel measurements for moderate to large water drops.

The model yields the peculiar asymmetric shape of raindrops: a singly curved surface with a flattened base and a maximum curvature just below the major axis. A close match was found between model shapes and profiles obtained from photos of water drops for diameters up to 5 mm. Coefficients are provided for computing raindrop shape as a cosine series distortion on a sphere.

In contrast to earlier models of raindrop shape for the oblate spheroid response to gravity (Green, Beard) or the perturbation response to the aerodynamic pressure for a sphere (Imai, Savic, Pruppacher and Pitter), the present model provides the appropriate large amplitude response to both the hydrostatic and aerodynamic pressures modified for distortion. In addition, the new model can be readily extended to include other pressures such as an electric stress.

1. Introduction

A large number of experimental and theoretical investigations on the shape of raindrops falling at their terminal velocities have been reported in the literature. High-speed photographs reveal that a large raindrop falling through the air exhibits a characteristic asymmetric shape having a flattened base and a smoothly rounded top. A small raindrop appears to have the symmetrical distortion of an oblate spheroid, whereas a drizzle drop looks spherical.

Current motivation for the research on raindrop shape is the need to understand depolarization of electromagnetic waves in rain. Depolarization degrades communication signals by cross-polar interference, but depolarization can also be a source of information about rainfall characteristics. As a consequence, there have been numerous studies on the effects of raindrop shape on the propagation of microwaves in communication links and on backscattering of microwaves as detected by weather radars (for review articles see Oguchi, 1981; Olsen, 1981; Rogers, 1984). In two recent studies the distortion of very large raindrops has been increased significantly over standard values to fit radar polarization data from storms (Caylor and Illingworth, 1986; Sachidananda and Zrnić, 1986) based on aircraft measurements of raindrop shape (Cooper et al., 1983; Chandrasekhar et al., 1984). Thus, our knowledge of the shape and distortion of raindrops is currently undergoing a reevaluation.

Experimental work on the shape of drops falling in air apparently originated with the wind tunnel studies of Lenard (1904) who speculated that internal circulation and surface tension were the key factors in drop deformation. [Earlier theoretical work of Bashforth and Adams (1883) focused on the effects of the internal hydrostatic pressure in producing sessile and pendant drops.] Modern experimental research on raindrop shape began with the wind tunnel studies of Blanchard (1950) and Magono (1954). More recent work with a refined wind tunnel (Pruppacher and Beard, 1970; Pruppacher and Pitter, 1971) has provided more detailed information on axis ratio as a function of raindrop size. Wind tunnel studies have also shown that large electrostatic distortions are likely for raindrops in thunderstorms (Richards and Dawson, 1971; Rasmussen et al., 1985).

Spilhaus (1948) provided a theoretical estimate of raindrop shape and suggested that the flattening of large raindrops is due to the aerodynamic pressure. He considered the raindrop as an ellipsoid but used an incorrect relationship in determining the pressure increment due to surface tension. A more extensive theory was developed by Imai (1950) who calculated the axis ratio of raindrops in potential flow using the linearized form

* Also affiliated with the Climate and Meteorology Section, Illinois State Water Survey.

of Laplace's equation. Imai disregarded the internal hydrostatic pressure and the external viscous effects to produce drops with the shape of an oblate spheroid for small deformation. Savic (1953) expressed the linearized form of Laplace's equation as an orthogonal series of $\cos(n\theta)$ and used a measured aerodynamic pressure distribution for a sphere (Flashbart, 1927). By solving a system of linear equations, he obtained the shape coefficients for falling drops. Savic found that the distortion depended on the aerodynamic pressure but was independent of the internal hydrostatic pressure.

McDonald (1954a), calculated the aerodynamic surface pressure from photographs of Magono (1954) and roughly estimated the magnitude of internal circulation at the waist. He concluded that the hydrostatic pressure due to gravity was an important component of drop shape, and that the separation in the airflow around a raindrop was primarily responsible for the asymmetry of large raindrops. Pruppacher and Pitter (1971) made some adjustments to Savic's model and used the measurements of Fage (1937) for a sphere. They obtained very similar results to Savic's and found fairly good agreement with wind tunnel measurements of drop axis ratio. Green (1975) estimated the axis ratio by simply considering the balance between surface tension and hydrostatic pressure at the equator of an oblate spheroid. Beard (1982, 1984) showed that axis ratios could be obtained from a potential energy balance using only gravity and surface energy. These simple theories of gravitational distortion also give fairly good agreement with wind tunnel measurements.

In spite of these modern theoretical and experimental investigations, the forces important to raindrop shape are not well understood. The perturbation models provide only an aerodynamic shape, and are of questionable value when applied to large amplitude distortions observed for raindrops greater than 3 mm diameter. The gravitational models are inappropriate for calculated shape since the forces on raindrops are only crudely approximated. Absent from previous models is the possible significant effect of internal circulation (Foote, 1969). And, existing theories of drop distortion by electric charges and fields do not include the circulations within and around drops. Thus, a principal motivation for our study is to solve the complicated problem of raindrop shape with due regard to the important forces. In the new model, the approach of Bashforth and Adams for the hydrostatic distortion has been expanded to incorporate an aerodynamic supporting pressure. The method of applying an empirical pressure distribution around a sphere, originally proposed by Savic, has been refined to include variations in the pressure distribution with Reynolds number and drop distortion. In subsequent research, we plan to make further improvements to the aerodynamic pressure distribution, and address electrostatic effects and, possibly, internal circulation.

2. Calculations of drop shape

There are five key factors that affect raindrop shape: surface tension, hydrostatic pressure, aerodynamic pressure, internal circulation and electric stress. The initial step in the development of the new model is a force balance along the surface of a raindrop among the first three factors. Possible subsequent development of the model, to include internal circulation and electric stress, is discussed in the conclusions.

The theoretical basis for drop shape is given by Laplace's pressure balance relating the curvature at each point on the surface to the internal and external pressures by

$$\sigma[1/R_1 + 1/R_2] = \Delta p \tag{1}$$

where σ is the surface tension, R_1 and R_2 are the principal radii of curvature, and Δp is the pressure across the interface. The curvature can be evaluated in the manner of Hartland and Hartley (1976) using a tangent angle coordinate system in a vertical plane through the center of the drop with the origin at the uppermost point of the surface as shown in Fig. 1. The principal variables are the arc length (s) and the angle (ϕ) between the tangent to the drop surface and the x-axis. The radius of curvature in the x–z plane is R_1 with length BP, and is defined by the differential relation between ϕ and the arc length as $ds = R_1 d\phi$. This curvature is therefore

$$1/R_1 = d\phi/ds. \tag{2}$$

The orthogonal radius of curvature, R_2, with length of AP, generates a horizontal arc through P as the triangle ACP is rotated about the z-axis. Since $x = R_2 \times \sin\phi$, this curvature is simply

$$1/R_2 = \sin\phi/x. \tag{3}$$

Laplace's equation is therefore

$$\sigma d\phi/ds + \sigma \sin\phi/x = p_i - p_e. \tag{4}$$

Two auxiliary equations in the tangent angle coordinate system are $dx/ds = \cos\phi$ and $dz/ds = \sin\phi$, as is evident from the differentials in the triangle shown on Fig. 1.

Laplace's equation is a nonlinear differential equation when expressed in terms of the coordinates x and z. It has no analytical solution for the effect of distortion pressures, even for axisymmetric drops. However, the problem of the hydrostatic distortion was of sufficient interest that the integration was carried out numerically over 100 years ago. The results were published by Bashforth and Adams (1883) on experiments and calculations of the shape of sessile and pendant drops. They determined the shape of a sessile drop, with a hydrostatic pressure of $\Delta\rho gz$ by assuming an external pressure of $p_e = 0$ and an internal pressure of $p_i = (p_i)_t + \Delta\rho gz$. [At the top the curvatures are equal from axisymmetry so that $(p_i)_t = 2\sigma/R_t$ where R_t is the radius of curvature.]

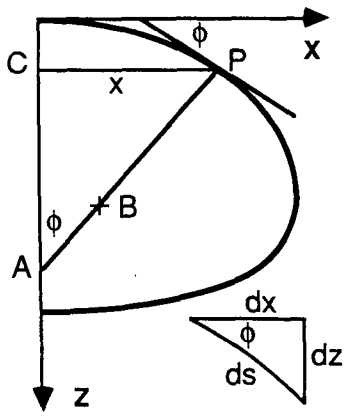

FIG. 1. Diagram of curve for the drop surface in the x–z plane with radius of curvature R_1 given by BP and R_2 by AP (both lying on the perpendicular to the curve at P).

The shape is calculated by forward integration of $ds/d\phi$ for assumed values of the initial curvature at the top. For convenience, we use a dimensionless form of the sessile drop equation given by

$$\sigma d\phi/dS = -\sin\phi/X + 2/C + Z \tag{5}$$

where $dS = bds$, $X = bx$ and $C = bR_t$ and $Z = bz$, and where the physical properties are specified by $b = (\Delta\rho g/\sigma)^{1/2}$ having units of inverse length. The integration is terminated at a tangent angle of 180° at the outer edge of the flat base where the drop height (h) and volume have been completely determined. At this point the integral of vertical force from internal pressure over the curved surface reaches zero, and therefore the net force from the uniform pressure over the base ($2\sigma/R_t + \Delta\rho gh$) is equal to the drop weight. The base is flat because the external pressure of the support is also equal to $2\sigma/R_t + \Delta\rho gh$.

Results for sessile drops can be found in Hartland and Hartley (1976) with the shape tabulated for particular values of C in terms of ϕ, S, X, Z, and the dimensionless surface area and volume. The shape for certain drop sizes can be found by locating the appropriate dimensionless volume.

3. Simple calculations using the new model

A more challenging problem is to calculate the shape of a raindrop, since both hydrostatic and dynamic pressures must be treated. We have extended the method of Bashforth and Adams for a sessile drop to a raindrop by including the external aerodynamic pressure (p_a). Laplace's equation is expressed in the tangent angle coordinate system as

$$\sigma d\phi/ds + \sigma \sin\phi/x = (p_i)_t + \Delta\rho gz - p_a. \tag{6}$$

At the top $p_i = (p_i)_t$ and $p_a = (p_a)_t$, so that the initial curvature has the relation $2\sigma/R_t = (p_i)_t - (p_a)_t$. Therefore (6) can be rewritten as

$$\sigma d\phi/ds = -\sigma \sin\phi/x + 2\sigma/R_t + \Delta\rho gz + (p_a)_t - p_a \tag{7}$$

with a dimensionless form given by

$$d\phi/dS = -\sin\phi/X + 2/C + Z + (\sigma b)^{-1}[(p_a)_t - p_a]. \tag{8}$$

Following Savic (1953) the aerodynamic pressure is based on the measured distributions around a sphere in terms of a polar coordinate angle θ, with $\theta = 0$ at the lower pole

$$p_a = \tfrac{1}{2}\rho V^2 \kappa(\theta) \tag{9}$$

where $\kappa(\theta)$ is the dimensionless pressure distribution. Since the aerodynamic pressure at the top is $(p_a)_t = (1/2)\rho V^2 \kappa_t$ and $\kappa_t = \kappa(\pi)$, Eq (8) can be rewritten as

$$d\phi/dS = -\sin\phi/X + 2/C + Z - \mathrm{We}[\kappa(\theta) - \kappa(\pi)]/A \tag{10}$$

where $\mathrm{We} = a\rho V^2/2\sigma$ is the Weber number, $A = ba$ is the dimensionless drop radius, and a is the radius of an equivalent volume sphere.

Equation (10) can be solved by forward integration from the upper to lower poles. The initial value of the curvature is simply $d\phi/dS = 1/C$, since $Z = 0$, $\kappa(\theta) - \kappa(\pi) = 0$, and $d\phi/dS = \sin\phi/X$. The appropriate lower boundary value is reached through the constraint of mechanical equilibrium between the weight of the drop and the support. The accumulated downward force can be computed by integration of the volume element $\pi x^2 dz$ (times $\Delta\rho g$) or by integration of the internal pressure acting on the surface with a vertical component given by $df = -2\pi x p_i \cos\phi ds = -2\pi p_i x dx$. Thus the lower pole is reached in the integration just as the net weight of the drop is completely supported by an external force. [The external force can be calculated from summing the elements $2\pi p_e x dx$.]

a. *Sessile drop shape*

In our first set of calculations we set the Weber number to zero in (10) to obtain the shape of a sessile drop with the assumption that the weight of the drop was supported by a thin film of air above a fixed horizontal plane. This conceptual model allows the surface tension along the base of the drop to be unaffected by the support, and is equivalent to a perfectly nonwettable support with a contact angle of 180°. Integration was begun at the upper pole using the boundary condition for the dimensionless curvature given by $d\phi/dS = 1/C$. As the integration proceeded from the upper pole, the curvature in the x–z plane continually increased. The integration was terminated at a tangent angle of 180° where the drop shape and volume were completely determined.

An iterative method was used to determine the value of R_t necessary to achieve the appropriate volume for

a particular drop size. The integration method was a fourth order Runge–Kutta scheme. A small enough step size was specified so that agreement was obtained to 5 significant figures in the drop height with previously calculated results for sessile drops (Hartland and Hartley, 1976). No significant differences were found between results using our simple fourth order scheme and a fourth/fifth-order Runge–Kutta scheme with internal control of step and global errors (Forsythe et al., 1977).

Sessile drop shapes are shown in Fig. 2 for six drop sizes, d = 1, 2, 3, 4, 5 and 6 mm where $d = 2a$ is the diameter of the equivalent volume sphere. As described in the previous section the flat base is a result of the drop's weight acting on a horizontal supporting surface. The extent of the base area increases with the Bond number (Bo = $\Delta\rho g a^2/\sigma$), and drop size, since the hydrostatic pressure at the base increases with respect to the internal pressure ($2\sigma/R_t$). The axis ratio (α) for a sessile drop, shown in Table 1, is smaller than predicted by the hydrostatic effect in the oblate spheroid models of Green (1975) and Beard (1982). From the asymmetry about the horizontal axis in Fig. 2, it is evident that one effect of the extra volume in the lower half of a sessile drop is to increase the width of the drop when compared to an oblate model.

b. *Raindrop shape using p_a for a sphere*

For calculations of the aerodynamic effect we had to consider how to balance the weight of the drop against an upward force in order to obtain a closed drop shape. Although the weight of a drop falling at terminal velocity is supported entirely by the aerodynamic drag, only the normal component (i.e., the pressure drag) can be used in Laplace's equation of mechanical equilibrium. For raindrops the pressure drag is about 60% to 90% of the total drag based on estimates of the pressure drag and total drag on spheres, discussed in detail below.

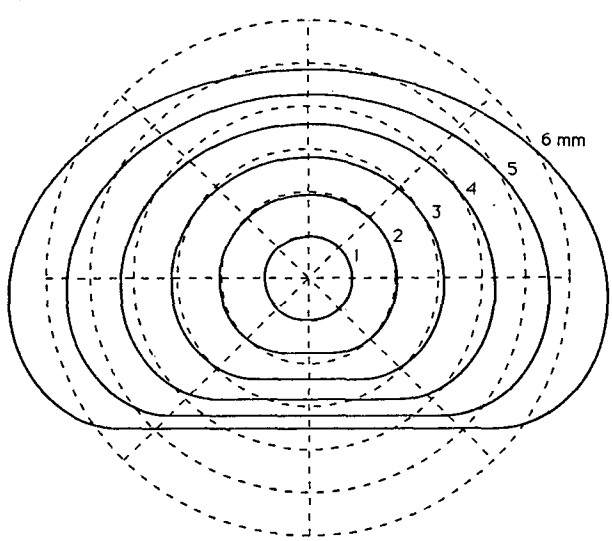

FIG. 2. Sessile drop profiles for d = 1, 2, 3, 4, 5 and 6 mm. Shown for comparison are dashed circles of diameter d divided into 45 degree sectors.

TABLE 1. Model results for raindrop axis ratios. Values in brackets have been interpolated from results at the nearest drop sizes.

	Aerodynamic models			Hydrostatic models		
d (mm)	Imai	Savic	Pruppacher and Pitter	Green	Beard	Sessile drop
1.0	0.96	—	[0.98]	0.98	0.98	0.97
2.0	0.88	[0.92]	[0.92]	0.92	0.92	0.90
3.0	0.61	[0.85]	0.85	0.84	0.85	0.82
4.0	—	—	0.76	0.77	0.77	0.75
5.0	—	—	0.70	0.71	0.69	0.67
6.0	—	[0.67]	0.66	0.65	0.62	0.61

The normal component of the drag in dimensionless form (the pressure drag coefficient) is given for a sphere by the integral of the dimensionless pressure from θ = 0 to 180°

$$C_{dp} = 2\int \kappa(\theta)\cos\theta\,\sin\theta d\theta. \tag{11}$$

In the range of Reynolds number applicable to larger raindrops (Re = 860–4830 for d = 2–8 mm) the pressure drag on a sphere increases with Reynolds number from about 81 to 92% of the total drag as determined from an empirical formula based on the measurements of Achenbach (1972)

$$C_{dp} = C_d[1 - B\,\mathrm{Re}^{-m}] \tag{12}$$

with B = 5.48 and m = 0.50. This formula is an extrapolation of the data trend in the 75 000–20 000 Reynolds number range and intersects the numerical results of LeClair et al. (1970) at Re $\approx$ 100 where C_{dp}/C_d = 0.46. However, at Re = 400 the extrapolation predicts a significantly higher value of C_{dp}/C_d than LeClair et al. (0.73 vs 0.58). Thus an interpolation formula was obtained by using end points from LeClair et al. at Re = 400 and Achenbach at 75 000. The use of the interpolation formula instead of Achenbach's decreases the pressure drag coefficient by only a few percent for larger raindrops (d > 3 mm).

We used (12) with B = 13.4 and m = 0.58 to estimate the pressure drag on a raindrop by assuming that the ratio C_{dp}/C_d for a sphere is the same for a raindrop. Since the drag on a raindrop is well approximated by the drag on an equivalent rigid spheroid (see, Beard, 1976), it is appropriate to calculate the pressure drag on a raindrop by this method. The equivalent volume diameter (d) is used to define the Reynolds number in (12). (The use of the Reynolds number based on the

horizontal major axis would change the value of C_{dp} by only 0.01.)

When we integrated the pressure distribution used by Pruppacher and Pitter (1971) for calculating raindrop shape (Fage, 1937), we found that the pressure drag was 0.45, higher than the *total* drag on a sphere in the range of Reynolds numbers (1500–5000) applicable to large raindrops (d = 3–8 mm). Although the distribution of Fage supposedly applies in the range from Re = 10^3–10^5 (Pruppacher and Klett, 1978), the actual measurement was made at Re = 1.6×10^5. At such high Reynolds numbers the total drag on a sphere is $C_d \approx 0.45$. Since Eq (12) predicts that $C_{dp} \approx C_d$, our integration of Fage's data to obtain the pressure drag is consistent with drag measurement for spheres at very high Reynolds number.

We could not find any measurements of the pressure distribution around a sphere for Reynolds number less than 6×10^4. It is apparently impractical to measure the pressure distribution for lower Reynolds numbers (assuming a standard wind tunnel measurement with a practical sphere size, e.g., see Maxworthy, 1969). The major difficulty appears to be that the stagnation pressure, as measured by a manometer, results in less than a 3 mm water displacement if the Reynolds number is less than 6×10^4.

To examine the suitability of Fage's pressure distribution at Re = 1.6×10^5 for Reynolds number of less than 10^4 we compared available measurements and numerical results for spheres in Fig. 3. There is little difference among results in most of the unseparated region ($\theta < 65°$). At larger angles the numerical result for steady-state flow at Re = 400 differs from the measurements having a notably broader dip and higher rear stagnation pressure. The distributions for high Reynolds number are rather flat behind the separation point which is a characteristic of a gradual pressure recovery for flow around a detached wake. Since a detached wake occurs for Re > 450 (see Beard, 1976), the pressure distribution in the wake for raindrops should more closely resemble the high Reynolds number curves than the numerical result for steady-state flow with an attached wake (Re = 400). The high Reynolds number curves predict dimensionless pressures (κ) within ±0.05 with only a few degrees variation in the location and breadth of the pressure dip. Small uncertainties in pressure and in the location of the minimum are not a primary consideration, since the major response of raindrop shape occurs from changes of considerably larger magnitude (for example, in applying the shape correction Γ_α discussed below). Based on these comparisons Fage's distribution appears to be a reasonable approximation to the flow around a sphere for Re = 10^3–10^5, although an adjustment may be desirable to obtain the appropriate pressure drag for a particular Reynolds number.

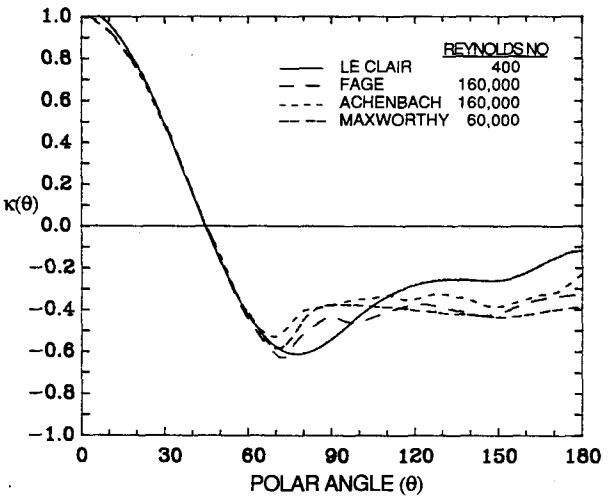

FIG. 3. The aerodynamic pressure (κ) as a function of polar angle (ϕ). Dashed curves show the distribution measured for a sphere for high Reynolds number with a detached wake. Solid curve show a numerical result for steady state with an attached wake.

The flow behind spheres is unsteady above about Re = 200, and therefore the use of Fage's averaged pressure distribution to calculate raindrop shape would not account for possible shape responses to pressure fluctuations in wake. Coupling is expected to be strongest where the oscillation period for the oblate-prolate mode is comparable to the eddy shedding period (Gunn, 1949). The two periods are comparable at $d \approx 0.9$ mm for water drops falling in air, but at $d = 2$ mm the eddy shedding frequency is an order of magnitude above the oscillation frequency. For larger raindrops eddy shedding is less coherent and has averaged frequencies corresponding to oscillations of very high harmonics (>10). Thus, the principal distortion of larger raindrops ($d \geq 1.5$ mm) should be the response to the steady-state pressure distribution or the average as obtained from Fage.

Calculations for the aerodynamic effect were first made for d = 5 mm using a cubic spline interpolation of the measured pressure distribution of Fage (1937). To close the drop shape at the lower pole the pressure drag was increased to equal the weight by increasing the amplitude of $\kappa(\theta)$. Since the amplitude of pressure distribution was artificially enhanced, the result should overestimate the distortion of a water drop falling in air. Although the distribution of Fage is the same as used by Pruppacher and Pitter (1971), it was assumed to apply to a distorted drop at the point on the surface having the same tangent angle as the sphere. It is shown in the next section that this assumption normalizes the pressure distribution for potential flow around oblate spheroids of any axis ratio. The pressure distribution of Fage, $\kappa(\theta)$, was therefore evaluated using $\kappa(\psi)$, where $\psi = \pi - \phi$ is the tangent angle referenced to the lower pole.

In the trial calculation for $d = 5$ mm, the amplitude of the pressure distribution was altered using a constant factor, $\Lambda\kappa(\psi)$, to obtain a pressure drag equal to the weight of the drop. The initial value of the curvature at the upper pole was readjusted until volume was conserved. Resultant curves of the drop surface in the vertical plane of symmetry are shown in Fig. 4 for $\Lambda = 0.74, 0.76, 0.78$ and 0.80. The amplitude of the pressure distribution, which was based on a sphere, had to be decreased ($\Lambda < 1$) to compensate for the increased pressure drag when applied to a distorted drop. It was possible by adjusting Λ to get as close to the z-axis as needed to adequately determine the volume and axis ratio or to make the cusp at the z-axis imperceptible on a plot of drop shape. ($\Lambda = 0.764$ was used to obtain the axis ratio to three significant figures: $\alpha = 0.746$.)

The axis ratios computed by the tangent angle method are $\alpha = 0.98, 0.93, 0.87, 0.81, 0.75$ and 0.69, for $d = 1, 2, 3, 4, 5$ and 6 mm, respectively. The results from the present model might be expected to represent a lower bound on the axis ratio for raindrops, because the distorting pressure from pressure drag was increased to balance the weight. Nevertheless, the axis ratios are larger (drops less distorted) than other results shown in Table 1. In the following sections the axis ratio is reduced (the distortion increased) to more reasonable values by modifying the pressure distribution for the effect of the shape.

The above results for raindrops show higher axis ratios (less distortion) than for sessile drops in Table 1. This comparison would seem to indicate that the effect of adding the aerodynamic to the hydrostatic distortion is to lessen the distortion. However, both the sessile drop and the aerodynamic calculations use the same total supporting force so that the comparison actually shows how axis ratios are affected by *differing forms* of the supporting pressure. The larger axis ratio for the aerodynamic support is principally an outcome of the greater drop height produced by the rounded base (compare the 5 mm drops in Figs. 2 and 4).

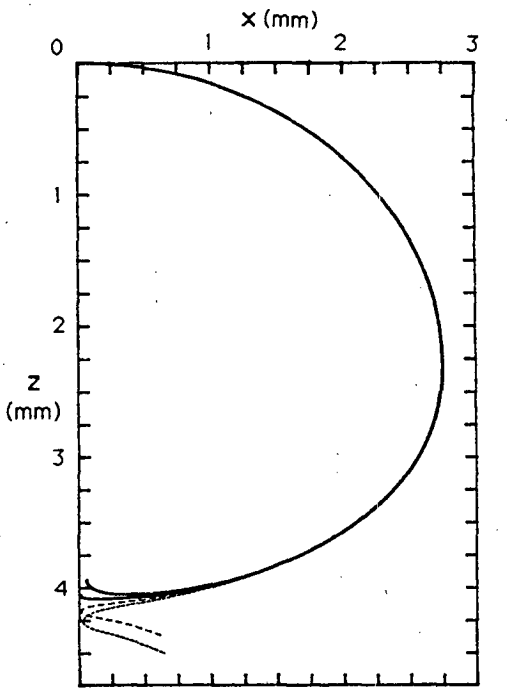

FIG. 4. Drop shapes in response to the hydrostatic and aerodynamic pressures for $d = 5$ mm. The four curves near the lower pole are for different values of Λ in the modified pressure distribution, $\Lambda\kappa(\psi)$, with values of Λ that increase (0.74, 0.76, 0.78, 0.80) for the successively lower curves. The best value of Λ is 0.764 to three significant figures.

4. Calculations adjusted for shape

Model calculations discussed to this point are based on the measured pressure distribution for a sphere at high Reynolds number using an adjustable amplitude factor (Λ) to satisfy the lower boundary condition. No correction has been made to the pressure distribution for the effect of raindrop shape. As the distortion increases, the air velocity around the side of the drop increases thereby lowering the pressure minimum.

a. Pressure distribution around a spheroid

We have modified the measured pressure distribution around a rigid sphere at large Reynolds number for the effect of raindrop distortion by applying different adjustments in the unseparated and separated flow regions. Potential flow is used to determine the change in pressure applicable to unseparated flow in the lower portion of the raindrop. Although a series solution for potential flow can be determined for the computed axisymmetric shapes (Grover and Beard, 1974), it is much simpler as a first approximation to consider the change in pressure for an oblate spheroid. For this purpose the velocity field was evaluated using the appropriate boundary conditions in the general form of the stream function given by Happel and Brenner (1965) in oblate spheroid coordinates (ξ, η). The distribution of dynamic pressure at the surface was then determined from Bernoulli's principal (the quantity $p + 0.5\rho U^2$ is a constant along streamlines) resulting in $p = 0.5\rho V^2 - 0.5\rho U_\eta^2$. The pressure is given in dimensionless form by

$$\chi_\alpha(\eta) = 1 - U_\eta^2/V^2. \tag{13}$$

The solution for the surface velocity is

$$U_\eta = V \sin\eta[(\lambda^2+1) - \sin^2\eta]^{-1/2}[(\lambda^2+1)\cot^{-1}\lambda - \lambda]^{-1} \tag{14}$$

where η is related to the polar coordinate angle by $\tan\eta = \alpha\tan\theta$, and where λ is the ratio of the axis ratio to the eccentricity: $\lambda = \alpha/\epsilon$, $\epsilon = (1-\alpha^2)^{1/2}$.

To obtain a pressure distribution corrected for shape we assumed that the fractional deviation of the corrected pressure distribution from Fage's measured distribution would be the same as the fractional deviation in potential flow of an oblate spheroid from a sphere. Using the stagnation point as a reference, this relationship is $[1 - K(\psi)]/[1 - \kappa(\psi)] = [1 - \chi_\alpha(\psi)][1 - \chi(\psi)]$, where $K(\psi)$ is the corrected pressure, and where $\chi = 1 - \frac{9}{4}\sin^2\psi$ is the pressure distribution for potential flow around a sphere. [The fractional deviations were calculated at the same tangent angle (ψ) for consistency with the method used in applying the aerodynamic pressure to computed drop shape.] The corrected pressure at a particular axis ratio and tangent angle was found from

$$K(\psi) = 1 - \Gamma_\alpha[1 - \kappa(\psi)] \tag{15}$$

where, from potential flow

$$\Gamma_\alpha = [1 - \chi_\alpha(\psi)][1 - \chi(\psi)]^{-1} = [U_\eta(\psi)/V]^2\left[\frac{9}{4}\sin^2\psi\right]^{-1}. \tag{16}$$

The value of the spheroid velocity at the same tangent angle as the sphere was found using $\tan\eta = \alpha^{-1}\tan\psi$ and replacing $\sin^2\eta$ in (16) with $\sin^2\psi[\alpha^2\cos^2\psi + \sin^2\psi]^{-1}$. When this substitution is made the adjustment for the potential flow velocity is found to be only a function of axis ratio,

$$\Gamma_\alpha = \frac{4}{9}\lambda^{-2}[(\lambda^2 + 1)\cot^{-1}\lambda - \lambda]^{-2} \tag{18}$$

since $\lambda = \alpha[1 - \alpha^2]^{-1/2}$. The fact that (18) is independent of ψ demonstrates that the tangent angle assumption normalizes the pressure distributions for spheroids. Thus, the use of the tangent angle for computing drop shape is consistent with theory.

In the separated flow region of the raindrop, the pressure recovers only slightly as a result of the gradual deceleration of the flow outside a detached wake. The potential flow correction if applied downstream from the pressure minimum would cause large, unrealistic variations in the pressure gradient. To obtain the pressure in the wake, Γ was held at the constant value that yielded the appropriate pressure drag.

For the purpose of drop shape calculations, Fage's data was first interpolated to 1° intervals using a cubic spline method. Then the measured distribution around the sphere was adjusted for the effect of distortion using (16). In the unseparated flow region from 0 to 72°, the potential flow correction (Γ_α) given by (18) was applied up to the pressure minimum in Fage. In the wake from 88° to 180°, a constant adjustment of $\Gamma = \Gamma_d$ was chosen to obtain the appropriate pressure drag by integration of the entire pressure distribution [$K(\psi)$] normal to the surface of an oblate spheroid. The pressure drag was specified by (12) using C_d for the particular raindrop. (The value of Γ in the region from 72° to 88° was chosen to be a simple linear transition between Γ_α and Γ_d.)

Shown in Fig. 5 are the pressure distributions used in calculating the adjusted distribution for a raindrop of $d \approx 5$ mm with an assumed axis ratio of 0.71 and Reynolds number of 3100. Potential flow distributions are given for a sphere ($\alpha = 1$) and an oblate spheroid ($\alpha = 0.71$). The measured distribution of Fage for a sphere is the curve labeled as $\alpha = 1$ and Re = 160 000. The potential flow adjustment was applied from 0° to 72° so that the difference between resultant pressure for the raindrop and Fage's measured pressure for a sphere was scaled by the difference between potential flows for the oblate spheroid and the sphere. The adjustment in the wake Γ_d from 88°–180°, using a linear transition between Γ_α and Γ_d from 72°–88°, was chosen for an appropriate pressure drag on the raindrop.

b. *Raindrop shape using adjusted p_a*

The aerodynamic pressure distribution corrected for the effect of shape, $K(\psi)$, is illustrated by examples in Fig. 6 for axis ratios of $\alpha = 0.9$, 0.8 and 0.7 with assumed Reynolds numbers of 1000, 2000 and 3000 (corresponding to raindrops of $d \approx 2.2$, 3.6 and 5.0 mm). Also shown for comparison is the pressure around a sphere ($\alpha = 1$) measured by Fage (1937) but adjusted for an appropriate pressure drag at a Reynolds number of 500. The amplitude of the aerodynamic

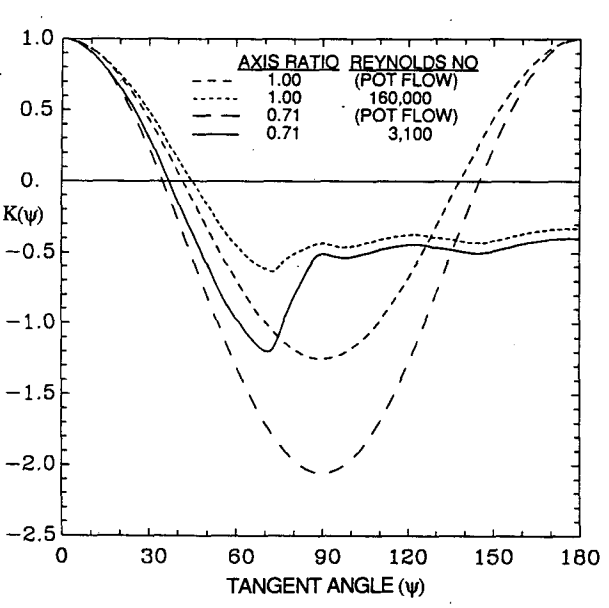

FIG. 5. The aerodynamic pressure (K) as a function of tangent angle (ψ). The curves are shown for potential flow around a sphere, the measured distribution around a sphere at high Reynolds number, for potential flow around an oblate spheroid with $\alpha = 0.71$, and for the adjusted distribution for a raindrop ($d \approx 5$ mm) assuming Re = 3100 and $\alpha = 0.71$.

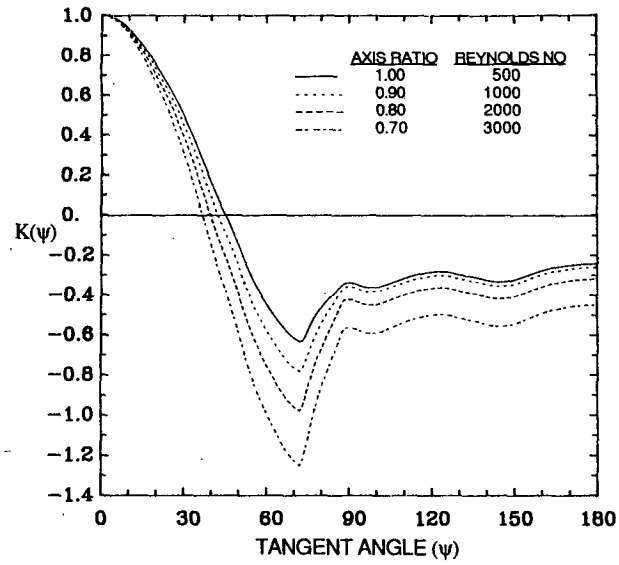

FIG. 6. The dynamic pressure (K) around a spheroid as a function of tangent angle (ψ). Curves are shown for α = 0.9, 0.8 and 0.7 corresponding to Re = 1000, 2000 and 3000. Also shown for comparison is the pressure distribution around a sphere (α = 1.0) adjusted to Re = 500.

distributions for raindrops becomes progressively larger with distortion.

The shape was first calculated for d = 5 mm using the aerodynamic pressure distribution based on an assumed axis ratio of $\alpha' = 0.7$. In order to obtain a closed drop shape the drag was also increased to balance the weight using a pressure distribution given by $\Lambda' K(\psi)$. [For the shape adjusted pressure distribution we use the notation Λ' for the amplitude factor and α' for the resultant axis ratio.] The amplitude factor for the 5 mm raindrop ($\Lambda' = 0.74$) was practically the same as that used for the sphere ($\Lambda = 0.76$). However, the aerodynamic pressure adjustment for shape (Γ_α) was significantly greater than unity so the axis ratio ($\alpha' = 0.704$) was appreciably lower than the result based on the pressure distribution around a sphere ($\alpha = 0.746$).

Results for the axis ratio (α') are given in Table 2 for d = 1 to 8 mm along with the raindrop size parameters (Re, Bo, We, C_{dp}/C_d). Also shown are parameters used for the shape calculations: the pressure adjustments for shape (Γ_α, Γ_d) and the amplitude factor (Λ'). The adjustment in the unseparated flow region (Γ_α) is based on potential flow around an oblate spheroid and so is a function of only the axis ratio. The adjustment in the wake (Γ_d) is used to obtain a pressure drag over an oblate spheroid which is an appropriate fraction of the total drag using (12). The amplitude factor for the pressure distribution (Λ') is large for small raindrops to compensate for the smaller value of C_{dp}/C_d. [Λ' is the factor that increases the pressure drag to equal the weight.] The value of Λ' is monotonic decreasing with increasing drop size as pressure drag becomes a larger fraction of the drop weight. However, Λ' becomes less than unity for $d > 2$ mm because the pressure drag over the resultant drop shape increases with distortion.

In these calculations the amplitude of the pressure distribution was increased to balance the weight, thereby artificially enhancing the distortion of a water drop falling in air. This "increased drag" method should provide a lower bound on axis ratios. An upper bound on the axis ratio was calculated by retaining the appropriate pressure drag but reducing the weight of the drop. A balance was obtained by first reducing the effective mass of the drop, a quantity proportional to $\Delta\rho$, so that the ratio of the reduced mass to the effective mass was the same as the ratio of the pressure drag to the total drag. The inverse length for use in the dimensionless form of Laplace's equation, became

$$b = [(C_{dp}/C_d)\Delta\rho g/\sigma]^{1/2}. \tag{19}$$

In order to close the drop shape at the lower pole it was still necessary to use an adjustable amplitude factor for the shape corrected pressure distribution, $\Lambda'' K(\psi)$, so that the pressure drag over the resultant drop shape was the appropriate fraction of the total drag. [The notation Λ'' and α'' is used for the "reduced weight" method.]

The results of the shape calculations for the upper and lower bounds on the axis ratios are shown in Table

TABLE 2. Raindrop size parameters (Re, Bo, We, C_{dp}/C_d), and model axis ratios (α') with the pressure distribution adjusted for drag and distortion (Γ_α, Γ_d, Λ').

d (mm)	Re	Bo	We	C_{dp}/C_d	Γ_α	Γ_d	Λ'	α'
1.0	263	0.0334	0.0651	0.532	1.016	0.936	1.802	0.978
2.0	863	0.1338	0.352	0.734	1.071	0.939	1.180	0.917
3.0	1593	0.301	0.799	0.814	1.153	0.961	0.950	0.842
4.0	2335	0.535	1.288	0.851	1.256	0.997	0.833	0.765
5.0	3012	0.836	1.713	0.871	1.383	1.050	0.778	0.694
6.0	3625	1.204	2.069	0.884	1.535	1.110	0.749	0.628
7.0	4229	1.639	2.414	0.894	1.711	1.168	0.723	0.566
8.0	4833	2.141	2.759	0.902	1.942	1.229	0.691	0.508

3. The constant (Λ'') used to adjust the pressure drag over the resultant shape is nearly unity for small raindrops because no adjustment to the pressure drag is required for a sphere to obtain a force balance with the reduced weight. A stronger adjustment is needed for larger raindrops to correct the pressure drag, based on an oblate sphere, for the resultant asymmetric drop shape. The corrections (Γ_α, Γ_d) to the pressure distribution for the effect of drop shape for reduced weight method are not shown since they differ only slightly from those for the increased drag method shown in Table 2.

The axis ratios in Table 3 for the upper bound (α'') are higher than the lower bound ($\hat{\alpha}$) by $\Delta\alpha = 0.010$ to 0.028 with $\Delta\alpha$ increasing with raindrop diameter from 1 to 8 mm. The uncertainty in the model results can be stated as $\alpha \approx \hat{\alpha} \pm \delta\alpha$ where $\delta\alpha \leq 0.014$. Thus, the present model predicts axis ratios with about a 1% uncertainty.

c. Raindrop shape using an intermediate force method

In order to test the sensitivity of the model axis ratios to the increased drag method and the decreased weight method, we repeated calculations for all drop sizes using the mean of the distorting forces. We were particularly interested in seeing whether an axis ratio calculated using a mean forcing (α) would be close to the mean axis ratio for the upper and lower bounds ($\hat{\alpha} = 0.5\alpha' + 0.5\alpha''$). In addition, it would be more satisfactory for comparisons of our result with other model shapes (and with observed shapes) to use calculated shape parameters for axis ratios appropriate for an intermediate forcing.

In these calculations the intermediate values for the distorting force were obtained by simply reducing the effective weight of the drop to the mean value determined from the effective weight and the fraction of the effective weight given by C_{dp}/C_d. To represent the intermediate forcing we used the factor $c' = 0.5\,(1 + C_{dp}/C_d)$ in (20) to obtain an inverse length given by

$$b = [c'\Delta\rho g/\sigma]^{1/2}. \tag{20}$$

An amplitude factor (Υ) was used with the shape corrected distribution, $\Upsilon K(\psi)$, to satisfy the lower boundary condition.

The results of calculations using the mean forcing are shown in Table 3. In addition to the axis ratio for the mean ($\hat{\alpha}$) and the mean forcing (α), values are given for the shape correction factors (Γ_α, Γ_d) and the amplitude factor (Υ). Since the factors Γ_α and Γ_d are shape dependent, the values from the mean forcing in Table 3 are practically the same as those for the lower bound in Table 2. Because of the intermediate forcing, the amplitude factor for adjusting the pressure drag (Υ) is intermediate to values for Λ' and Λ'' in Tables 2 and 3. The computed axis ratio α for the intermediate forcing is essentially the same as the mean $\hat{\alpha}$ with a maximum difference of 0.001. The difference between the two estimates of the mean axis ratio is much smaller than the range between the upper and lower bounds ($\Delta\alpha$), since $|\alpha - \hat{\alpha}|/\Delta\alpha < 0.1$.

The computed shapes in the vertical plane of symmetry are shown to relative scale in Fig. 7 for $d = 1$ to 6 mm from the mean forcing method. The drop shapes were placed with the center of mass at the origin of the polar coordinate diagram with corresponding dashed circles of radius a for each drop size. A common feature of these shapes is that the curvature ($1/R_1$) is positive everywhere, and therefore the cross sections in Fig. 7 are equivalent to drop profiles. Another common feature is that the maximum in the curvature, most clearly seen in the larger raindrops, lies just below the maximum horizontal chord.

5. Discussion of model results

a. Axis ratio comparisons

There are a considerable number of experimental measurement of the axis ratio, the simplest quantitative indicator of drop distortion. The data shown in Fig. 8 were obtained mostly from photographs of water drops suspended by air in vertical wind tunnels. Although care was used in obtaining the equilibrium axis ratios, there remained some unavoidable scatter from transient distortions excited by the various means used to stabilize the drop position and by pulsations in the

TABLE 3. Results from raindrop model. Values shown are Λ'' and α'' for the reduced weight method, α' for the increased drag method, $\hat{\alpha}$ for the mean $[0.5(\alpha'' + \alpha')]$, and Γ_α, Γ_d, Υ', and α for the mean forcing method.

d (mm)	Λ''	α''	α'	$\hat{\alpha}$	Γ_α	Γ_d	Υ'	α
1.0	0.975	0.988	0.978	0.983	1.012	0.937	1.392	0.983
2.0	0.898	0.938	0.917	0.928	1.061	0.940	1.042	0.928
3.0	0.808	0.867	0.842	0.854	1.141	0.961	0.882	0.853
4.0	0.744	0.792	0.765	0.779	1.241	0.998	0.790	0.778
5.0	0.711	0.722	0.694	0.708	1.359	1.051	0.746	0.708
6.0	0.694	0.657	0.628	0.642	1.498	1.112	0.723	0.642
7.0	0.677	0.595	0.566	0.581	1.663	1.170	0.701	0.581
8.0	0.659	0.536	0.508	0.522	1.878	1.222	0.678	0.521

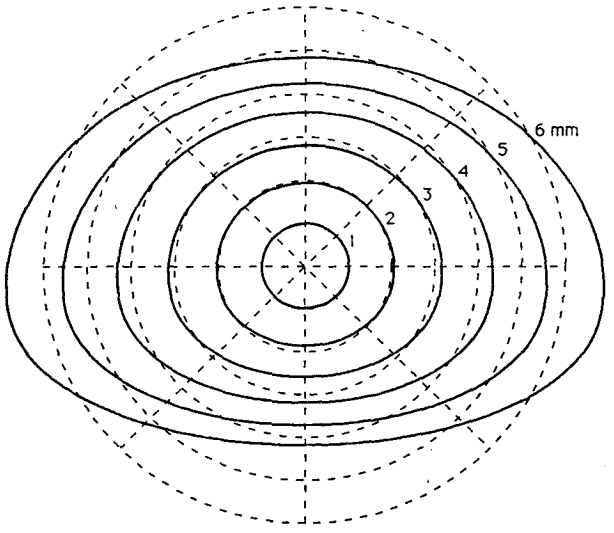

FIG. 7. Computed shapes for d = 1, 2, 3, 4, 5 and 6 mm with origin at center of mass. Shown for comparison are dashed circles of diameter d divided into 45 degree sectors.

airflow. Transient distortions are evident from the photographs of Magono (1954) for the two sizes near d = 6 mm (these photos are more clearly reproduced in McDonald, 1954b). The larger drop is less distorted (d = 6.5 mm, α = 0.64) than the smaller drop (d = 6 mm, α = 0.62), primarily because of changes in curvature at the lower pole. The base of the larger drop has a small extended region whereas the base of smaller drop is excessively flattened. This variation in the curvature at the lower pole for drops of nearly the same size is suggestive of an oscillating base. In contrast the photographs in Pruppacher and Beard (1970) do not show obvious signs of oscillations.

The wind tunnel study of Brook and Latham (1968) demonstrated that large amplitude oscillations can shift the axis ratio, on the average, significantly above equilibrium values. Theoretical support for these observations is found in the oscillation model studies, and show amplitude and mode dependences in the shift from equilibrium axis ratios (e.g., Beard, 1984). Thus, it is unfeasible to obtain a reliable fit to the experimental measurements shown in Fig. 8 because of likely bias from oscillations. However, the data of Pruppacher and Beard for very large drops should probably be given the more weight than Pruppacher and Pitter since the scatter is significantly smaller. The former measurements were made without the use of an upstream grid to stabilize the horizontal position of the drops, and thus were free of turbulence known to induce large amplitude oscillations.

The measurements of Best were made using an 11 meter fall column (see, Lane and Green, 1956). This distance is sufficient to achieve terminal velocity to

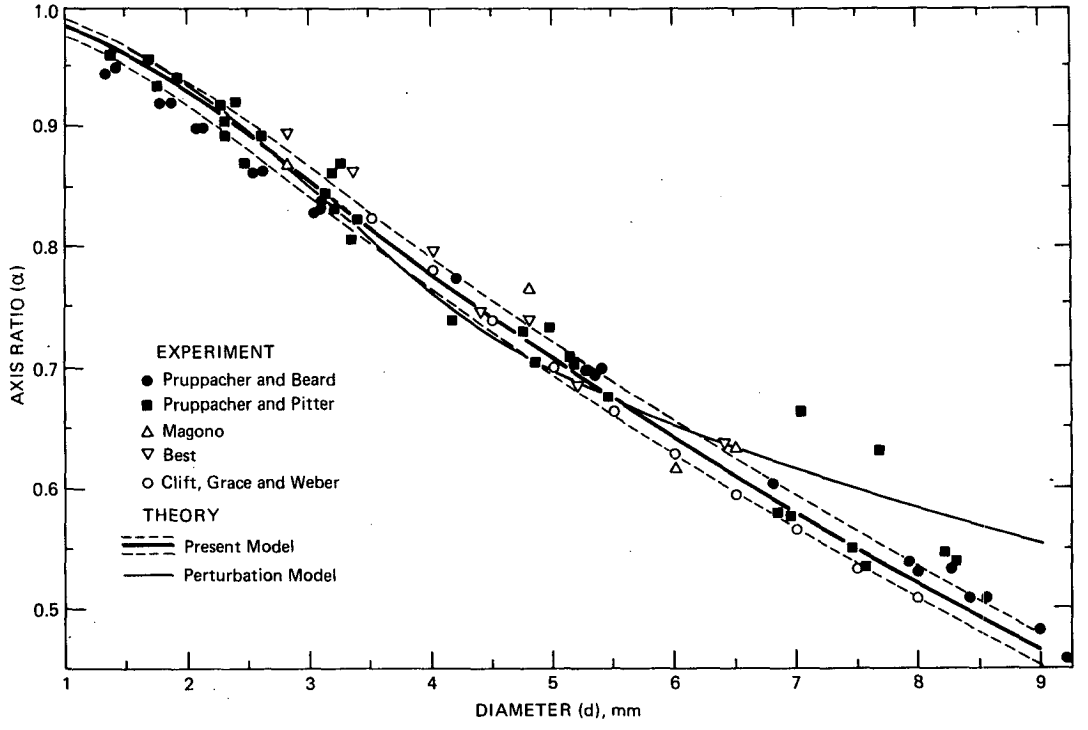

FIG. 8. Experimental and model results for axis ratio (α) as a function of drop size (d). The dashed lines show present model results for upper and lower bounds.

within about 3% (Beard, 1977). However, the response time for equilibrium shape and for damping of oscillations, induced by the dripper, is of the same order as the fall time. For example, the fundamental mode for a 5 mm diameter water drop only decays to 40% of its initial amplitude when accelerating from rest to 11 meters. Thus, these fall column data also show scatter due to oscillations. [The scatter is especially evident for the two measurements near $d = 5$ mm.]

In spite of the scatter in the measurements, it is clear from Fig. 8 that the mean forcing result from the new model follows the trend in measurements of the equilibrium axis ratio even for extremely large drops. In contrast, the perturbation model of Pruppacher and Pitter (1971) appears to overestimate the axis ratio for very large drops, and possibly underestimate the axis ratio near $d = 4$ mm. If we discount the two highest axis ratios from Pruppacher and Pitter for $d > 7$ mm then there is no experimental support for their theoretical result for very large drops. It is not really surprising that the perturbation calculations should diverge from reality at large distortion.

The new model results appear to be consistent with an empirical fit recommended by Clift et al. (1978) for drops falling in air. Their formula is based on data for drops of various liquids obtained by wind tunnel measurements reported in Garner and Lane (1959), and the fall column measurements of Reinhart (1964). [Data were not included from the more recent wind tunnel measurements of Pruppacher and Beard (1970) and Pruppacher and Pitter (1971).] The predicted axis ratios from the formula of Clift et al. are similar to the mean found in Garner and Lane. However, the original data in Garner and Lane and in Reinhart show considerable scatter with mean axis ratios consistently lower than the data for large water drops. Oscillations were noted in both papers, and the upstream grid in the wind tunnel apparently caused persistent oscillations since axis ratios had to be obtained from the average of 20 to 30 measurements at one size. Thus, there seems to be compensating biases in these measurements away from the equilibrium axis ratio for water drops: 1) higher axis ratios from the average of oscillating drops, and 2) lower axis ratios from the average over physical properties. With the assumption of roughly compensating errors from oscillations and physical property effects we would conclude that the empirical fit of Clift et al. is consistent with the new model results for equilibrium axis ratios. This possible support for the new model is worth noting because it originates from data other than the wind tunnel measurements shown on Fig. 8.

b. *Shape comparisons*

A more refined assessment of model results can be obtained by a direct comparison of shapes. For example, the raindrop shape for $d = 5$ mm with $\alpha = 0.708$ is shown in Fig. 9 (solid line) for comparison with other results for 5 mm drops: the sessile drop with $\alpha = 0.67$ (small dashes), the perturbation shape from the aerodynamic model of Pruppacher and Pitter with $\alpha = 0.70$ (lighter solid line) and the oblate distortion from the hydrostatic models of Green with $\alpha = 0.71$ (medium dashes). The drops shapes were placed with the center of mass at the origin of the polar coordinate diagram except for the shape from Pruppacher and Pitter which is a perturbation on the 5 mm sphere (large dashes) centered at the origin.

Although axis ratios are similar for these models, distinct shape differences are evident. In particular, the oblate shape is the only one that is symmetric about the horizontal plane through the center of mass with a maximum curvature at the side where the tangent angle is $\psi = 90°$. The sessile drop model is unique for its flat base with a maximum curvature at the edge of the base. The model of Pruppacher and Pitter is the only doubly curved surface and has a broad region of maximum curvature between the side and the base. When this shape is seen in profile, rather than as a cross section, the base appears flat like a sessile drop. The new model is a singly curved surface with a rounded base and a distinct maximum in curvature below the 90° tangent (see also Fig. 7). Shape features of the new model are closest to those observed for water drops supported in the air stream of a laminar wind tunnel (see, Pruppacher and Beard, 1970).

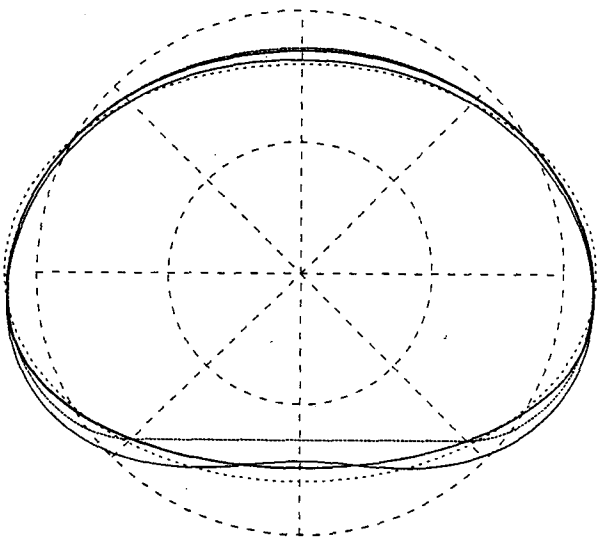

FIG. 9. Comparison of drop cross sections for $d = 5$ mm. The present result for a sessile drop is distinguished by a flat base (small dashes), whereas the present result for the mean forcing from the aerodynamic and hydrostatic pressures has a rounded base (solid line). The shape with a recurved base is the perturbation result of Pruppacher and Pitter (lighter solid line). Shown for comparison is an ellipse of axis ratio 0.71 (medium dashes), and circles (large dashes) scaled to 2.5 and 5 mm diameter with 45 degree sectors.

The various shapes in Fig. 9 reflect the underlying assumptions of the models. The hydrostatic models of Green and Beard have an oblate shape constraint and therefore lack the asymmetry found in the other models and observed for falling water drops. Of the three asymmetric results shown in Fig. 9, the sessile drop model is the most unrealistic representation of raindrop shape because the net force from the hydrostatic pressure is counteracted by a horizontal support. The height is diminished by the flat base resulting in axis ratios that are generally too small.

The model of Pruppacher and Pitter is based on a linearized form of Laplace's equation appropriate only for small distortion of a spherical drop (after Imai, 1953; Savic, 1953). The result is an axisymmetric perturbation produced by the aerodynamic pressure distribution for a sphere. The indentation at the base is a consequence of a large perturbation, seen to be about 30% of the radius in Fig. 9, from a response to the maximum external pressure in the region around the upstream stagnation point. It is not surprising to find a region of negative curvature in a perturbation model of drop shape with such a large amplitude distortion. Similar "dimples" are obtained using large amplitudes for the Rayleigh modes of oscillating drops [e.g., see Fig. 3 in Foote (1973) and Fig. 1 in Beard (1984)].

Model shapes for $d = 5$ mm are shown in Fig. 10 for comparison with profiles from drop photos in Magono (1954) for $d = 4.8$ mm ($\alpha = 0.76$) and Pruppacher and Beard (1970) for $d = 5.3$ ($\alpha = 0.71$). Digitized photos and a graphics computer were used to spline the edges. Since the axis ratio for the drop from Magono was higher than 0.71, the drop was uniformly stretched to obtain $\alpha = 0.71$. The adjustment did not affect particular details of this shape as characterized by the side-to-side asymmetry or the relative location of maxima and minima in curvature. Although both empirical profiles are slightly asymmetric with respect to the z-axis, the occurrence of the maxima in curvature in the lower part of the drops is similar to the profile from the new model. A superposition of the profiles shows maximum differences between the present model and either of the empirical shapes of only twice the width of the lines seen in Fig. 10. It is clear from Fig. 10 that the new model provides a noticeable improvement over the currently accepted model shape of Pruppacher and Pitter.

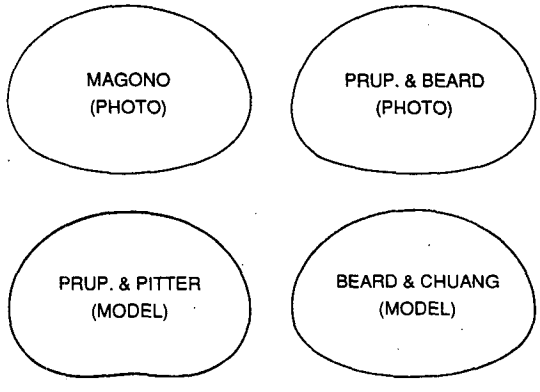

FIG. 10. Comparison of drop profiles (taken from photos) with model results for $d = 5$ mm.

Comparison with photos at smaller sizes (Magono, $d = 2.8$ mm; Pruppacher and Beard, $d = 2.7, 3.4$ mm) also indicates close agreement with present model. For larger sizes (Magono, $d = 6.0, 6.5$ mm; Pruppacher and Beard, $d = 5.8, 7.4, 8.0$ mm) the drop photos show bases noticeably flatter than the present model, although curvature of the bases appears to remain positive. In several photos the top is rounder, having a higher curvature, than the model. These variations in the photos are suggestive of oscillations (as noted for Magono in the first paragraph of section 5). If we assume that the shapes in the photos of larger drops are not grossly affected by oscillations, then the model for $d > 6$ mm underestimates the flattening of the base and, possibly, the curvature at the top.

A quantitative and global comparison of shapes can be made by considering the model shape coefficients given in Table 4 from a cosine series fit to the model results. A similar table appears in Pruppacher and Pitter and provides not only a means of comparison but a way to regenerate model shapes using

$$r = a[1 + \sum c_n \cos(n\theta)] \tag{24}$$

The undistorted sphere ($r = a$) is located at the center of mass of the drop.

Comparisons can be made by considering differences between shape coefficients, $\Delta c_n = c_n - c'_n$. Since the shape coefficients are the amplitudes for each $\cos n\theta$ contribution, the total difference between the two shapes at any particular angle cannot be greater than the sum of the absolute values of the differences, $\sum |\Delta c_n|$. [The sum of the differences, $\sum \Delta c_n$, is just the difference at $\theta = 0$.] The result for $\sum |\Delta c_n|$, using c_n from the present model and c'_n, from the model of Pruppacher and Pitter, is shown in the first column in Table 5. [The coefficients c_1 and c_{10} were excluded since they are zero in Pruppacher and Pitter.] This measure of discrepancy between the two models may be interpreted as the difference in the perturbations expressed as a percent of the spherical radius. For comparison, a measure of the perturbation, $\sum |c_n|$, from the present model (in percent of the spherical radius) is given in the second column. Therefore, $\sum |\Delta c_n| / \sum |c_n|$ provides a more sensitive measure of discrepancy between two shapes (given in the third column), since this quantity shows the discrepancy between the two models expressed as a percent of the perturbation rather than the spherical radius.

From the comparisons in Table 5 we conclude that there are considerable differences in shape for large raindrops between the new model and the perturbation

TABLE 4. Coefficients from cosine series fit to the computed shapes using the mean forcing for d = 0.5 to 6.0 mm. The shapes are obtained from the polar curve: $r = a[1 + \Sigma\, c_n \cos(n\theta)]$.

		Shape coefficients [$c_n \times 10^4$]									
d (mm)	$n = 0$	1	2	3	4	5	6	7	8	9	10
2.0	−131	−120	−376	−96	−4	15	5	0	−2	0	1
2.5	−201	−172	−567	−137	3	29	8	−2	−4	0	1
3.0	−282	−230	−779	−175	21	46	11	−6	−7	0	3
3.5	−369	−285	−998	−207	48	68	13	−13	−10	0	5
4.0	−458	−335	−1211	−227	83	89	12	−21	−13	1	8
4.5	−549	−377	−1421	−240	126	110	9	−31	−16	4	11
5.0	−644	−416	−1629	−246	176	131	2	−44	−18	9	14
5.5	−742	−454	−1837	−244	234	150	−7	−58	−19	15	19
6.0	−840	−480	−2034	−237	297	166	−21	−72	−19	24	23

model. Column 1 shows that the discrepancy is greater than about 5% of the spherical radius for drops larger than 4 mm diameter, and that the differences in the shape perturbations (column 3) is greater than 20% for these larger sizes. For small raindrops the discrepancy between the models decreases to a negligible percentage of the spherical radius (column 1) as the perturbation decreases (column 2). The errors in the perturbation model increase with perturbation size, becoming larger than 10% for perturbations larger than 10%.

The comparison also suggests that the shapes predicted by the two models converge for small raindrops. However, good convergence with the perturbation model of Pruppacher and Pitter was obtained only for the reduced weight method which yielded an upper bound on the axis ratio. (Comparison at d = 1 mm shown in Table 5 is based on the reduced weight method, whereas at other sizes the comparison is for the mean forcing method.) We note from Fig. 8 that the axis ratios of the perturbation model and the upper bound also converge below d = 2 mm. This apparent agreement between models at small distortion is consistent with Savic's finding (based on the linearized form of Laplace's equation) that the perturbation shape depends only on the aerodynamic forcing. The reduced weight method leaves the aerodynamic forcing unaltered and equivalent to the perturbation model. Further limitations for modeling the shape of small raindrops from the use of the steady state pressure distribution of Fage is discussed in sections 3b and 5e.

TABLE 5. Comparison of shape coefficients from new model result (c_n) with Pruppacher and Pitter (c'_n) for d = 1.0 to 6.0 mm. Deviations in percent are computed from $\Delta c_n = c_n - c'_n$.

d (mm)	$\Sigma\lvert\Delta c_n\rvert$	$\Sigma\lvert c_n\rvert$	$\Sigma\lvert\Delta c_n\rvert/\Sigma\lvert c_n\rvert$
1.0	0.05	1.0	5.0
2.0	0.7	6.3	11.4
3.0	1.8	13.3	13.3
4.0	4.8	22.1	22.7
5.0	8.6	29.0	29.6
6.0	13.0	37.1	35.0

c. *Dimples in the equilibrium shape of large raindrops?*

As an additional check on the shape of a large raindrop, we tested for the possible existence of a dimple in the base. The complete form of Laplace's equation (10) was used to determine the external pressure distribution required to produce a dimple using $f(X, Z)$ and $dS/d\phi$ from the perturbation model result of Pruppacher and Pitter for d = 5 mm (shown in Fig. 10). The computed external pressure distribution was of very large amplitude with a difference of $\Delta\kappa = 2.3$ between the lower and upper poles. If we assumed a rear stagnation pressure of $\kappa \approx 0.5$, consistent with Figs. 3, 5 and 6, the front stagnation pressure would be $\kappa \approx 1.8$. Thus, an unrealistically high base pressure is required to reproduce the perturbation dimple for a 5 mm equilibrium shape.

Photographs of drops supported by the air stream in a laminar wind tunnel show that drops as large as d = 8 mm have a rounded base with positive curvature (Pruppacher and Beard, 1970). In fact, essentially all photographs of water drops suspended in wind tunnels show a positive curvature at the base (Magono, 1954; Cotton and Gokhale, 1967; Spengler and Gokhale, 1973). One notable exception is a photograph in Koenig (1965) of a dimpled water drop of extreme size (having a horizontal dimension of 13 mm). A dimple at the base may be a feature of oscillating drops since photographic sequences show that the base tends to flatten at maximum distortion (Nelson and Gokhale, 1972; Musgrove and Brook, 1975). Although we do not doubt that indentations can occur in drops, it seems unlikely that they are a consequence of equilibrium forces on raindrops.

d. *Possible effects of internal circulation*

Circulation induced by tangential stress from the air flow around a falling drop can contribute to the equilibrium shape only through alterations of the normal stresses in Laplace's equation, i.e., through changes in the aerodynamic pressure (p_a) from the moving

boundary, and from the addition of a hydrodynamic pressure from internal circulation. Viscous flow analysis demonstrates that alterations from internal circulation in the pressure distribution and drag are of the order of the viscosity ratio, about 0.02 for water drops in air (Happel and Brenner, 1965). At moderately large Reynolds numbers LeClair et al. (1972) showed that the computed normal and tangential components of the drag for rigid and liquid spheres were altered by less than 1% from the effect of a moving boundary for a water sphere in air. In addition, the local value of p_a was reduced by only a few percent at the largest Reynolds number calculated (Re = 300, d = 1.1 mm). These findings are consistent with empirical evidence that the drag on small water drops falling in air is essentially the same as a rigid sphere of the same density. For larger (deformable) drops the best drag formulations are based on three dimensionless groups that, by dimensional analysis, apply only to noncirculating drops (see Beard, 1976). Thus, we can assume that the aerodynamic pressure distribution around a large raindrop is essentially unaffected by the motion of the surface, that is, p_a is well represented by the distribution around a rigid body of the same shape and Reynolds number.

Although the hydrodynamic pressure distribution from internal circulation is unknown at the Reynolds number for raindrops, scale analysis based on observed circulation velocities suggests that its magnitude is significant compared to the aerodynamic pressure. [The Weber number based on the maximum surface velocity for large water drops in air (LeClair et al., 1972) is about 30% of the Weber number based on the corresponding maximum airflow.] The hydrodynamic pressure distribution should be similar in shape to the aerodynamic pressure distribution, because the external and internal velocities are coupled directly through the stress boundary condition. Thus, as a first approximation, the effect of internal circulation can be included in Laplace's equation by a net dynamic pressure distribution with an amplitude somewhat reduced from p_a by the effect of internal circulation. This type of adjustment would reduce the distortion in a perturbation model of drop shape since it would reduce the aerodynamic forcing. However, it would not alter the drop shape in the present model, because the amplitude of the distribution is ultimately determined by the particular balance between weight and pressure drag (i.e., the increase drag, reduce weight or mean forcing methods). Thus, the present model is only sensitive to changes in the *form* of the dynamic pressure distribution. Possible variations from the form assumed for p_a due to internal circulation are unknown at large Reynolds numbers even for the simple geometry of liquid spheres. Thus, calculations on the effect of internal circulation on drop shape using the present model must await additional information on the hydrodynamic pressure distribution within drops.

6. Conclusions

The model computations of the lower and upper bounds on axis ratio were based on changes in amplitude of the external pressure distribution without a change in form. One method increased in pressure drag to balance drop weight and the other held the pressure drag constant and reduced the weight. Actual axis ratio should be intermediate to these results since one method artificially increases distorting force whereas the other artificially decreases it. The mean value of the lower and upper bounds was shown to produce the same axis ratios as the mean forcing method (whereby the weight reduction is only half the amount of the upper bound method). Therefore, it is thought that the axis ratio of falling drops having a natural balance between the total drag and the weight would differ only imperceptible from our model results (excluding inaccuracies from using an approximate pressure distribution). The uncertainty in the model axis ratios is relatively small when expressed as $\alpha = \alpha \pm \delta\alpha$ where $\delta\alpha \approx 0.01$.

The remaining theoretical uncertainties in the model is a matter of speculation on the magnitude of errors from the approximate nature of the dynamic pressure distribution. First, the hydrodynamic pressure from internal circulation has not been explicitly included in the model, but it is thought to play only a minor role in determining the form of the dynamic pressure distribution. Thus, the uncertainty in model drop shape from excluding internal circulation should be relatively small, since drop shape is insensitive to minor changes in the form of the pressure distribution. [For example, we found only a slight change in shape when the pressure distribution was altered from a sphere to an oblate spheroid—compare the 5 mm drop shapes in Figs. 4 and 7, and the corresponding empirical pressure distributions in Fig. 5 for α = 1 and 0.71.]

Second, the aerodynamic pressure has been approximated by the measured distribution around a sphere at high Reynolds number after using a potential flow adjustment for the symmetric oblate distortion in the unseparated flow region and a pressure drag adjustment in the wake. Uncertainty from the latter adjustment should be small because the drop shape would be insensitive to the minor pressure variations (and uncertainties) in the wake as revealed by Fig. 3.

The potential flow for the symmetric oblate distortion is a first step in the geometric correction to the aerodynamic pressure. An adjustment using potential flow for the *asymmetric* computed shape should result in a somewhat better approximation for the shape of very large raindrop. The shape might be expected to change in the same sense as the change for symmetric oblate correction to the sphere, that is, yield a flatter base. Thus, we expect a small systematic bias in our shapes (towards a rounder base) for $d > 5$ mm because

of the approximate potential flow adjustment for unseparated flow. However, the model axis ratios are not expected to be affected appreciably, since good estimates of axis ratio are obtainable for sizes beyond where models predict accurate shapes (e.g., consider the oblate spheroid models for d = 2–4 mm.] In fact, the model axis ratios appear to provide the best approximation to date for raindrops sizes up to d = 9 mm, because of the good agreement with wind tunnel observations.

The model shapes closely fit the profiles of rather large raindrops (d = 5 mm) with their distinctive asymmetric shapes. The shape coefficients are thought to best apply, however, to raindrops in the range from $d \approx$ 2 to 6 mm. At smaller sizes the results are based on the pressure distribution of Fage which is not as appropriate as the numerical results for steady state flow around a sphere. The axis ratios and shape coefficient for raindrop diameters less than about 1.3 mm would be improved if based on the distributions LeClair et al. (1970) as shown in Fig. 3 for Re = 400. We plan to compare our model with the perturbation model using the distributions of LeClair in the near future. We will determine how the present model results for the mean forcing (applicable for $d \geq$ 2 mm) merges with the reduced weight and perturbation results (applicable for $d \leq$ 1 mm). At sizes larger than about 6 mm diameter the empirical shapes have a flatter base than the model shapes. As a consequence of the above restrictions for the model shapes, the coefficients in Table 5 are given only for the range d = 2–6 mm.

It is of interest to note that the axis ratios in the present study for large raindrops are significantly higher than those used to fit data in two recent radar polarization studies (Caylor and Illingworth, 1986; Sachidananda and Zrnić, 1986). For example, the model value at d = 6 mm of α = 0.64 is significantly higher than either $\alpha \approx$ 0.55 inferred from the aircraft observations of drop shape by Cooper et al. (1983) or α = 0.60 observed by Chandrasekar et al. (1984). The present finding for axis ratios does not support the idea in the above radar studies that high differential reflectivities originate from raindrop equilibrium shapes, because it is unlikely that there are enough raindrops larger than d = 5 mm in the size distributions to yield radar average axis ratios of less than 0.7. Instead, we concur with Chandrasekar et al. that such large distortions should be attributed to raindrops containing unmelted ice rather than equilibrium shapes.

In the future we will extend our model by using potential flow about the asymmetric shape to refine the effects of drop shape on aerodynamic pressure distribution. After this improvement it should not be difficult to obtain the potential for the electric stress on a distorted drop and begin to model the effects of fields and charges on raindrop shape. In addition, calculations of the boundary layer will provide an external flow that can be used to drive internal circulation. It is hoped that our model for large amplitude distortions can form the basis for additional theoretical studies on forces that are thought to affect raindrop shape.

Acknowledgments. This material is based upon work supported by the National Science Foundation under Grant ATM84-19498.

APPENDIX

List of Symbols

A	dimensionless drop radius [$=ba$]
a	radius of equivalent volume sphere [$=d/2$]
b	inverse length intrinsic to Laplace's equation [$=(\Delta\rho g/\sigma)^{1/2} = a^{-1}\,\mathrm{Bo}^{1/2}$]
Bo	Bond number [$=\Delta\rho g a^2/\sigma$]
C	dimensionless radius of curvature at the upper pole [$=bR_t$]
C_d	total drag coefficient
C_{dp}	pressure drag coefficient
d	diameter of equivalent volume sphere
g	acceleration of gravity
h	distance from upper to lower pole
p_a	aerodynamic pressure
p_e, p_i	external pressure, internal pressure
R_1	principal radius of curvature (radius of curvature of drop in x–z plane)
R_2	principal radius of curvature (radius of curvature of drop orthogonal to R_1)
R_t	radius of curvature at top (upper pole)
Re	Reynolds number [$=\rho dV/\eta$, where η is the dynamic viscosity of air]
S	dimensionless arc length measured from upper pole [$=bs$]
V	terminal fall velocity
We	Weber number [$\rho a V^2/2\sigma$]
X	dimensionless x-coordinate [$=bx$]
Z	dimensionless z-coordinate [$=bz$]
α	axis ratio (ratio of height to maximum horizontal chord)
α', α''	lower, upper bound on axis ratio [$\Delta\alpha = \alpha'' - \alpha'$]
$\hat{\alpha}$, α	mean axis ratio [$\hat{\alpha} = 0.5(\alpha' + \alpha'')$], mean forcing axis ratio (α)
Γ_α	potential flow adjustment for distortion around oblate spheroid
Γ_d	pressure drag adjustment for distortion around oblate spheroid
Δp	pressure difference across drop surface [$=p_i - p_e$]
$\Delta\rho$	density difference between water and air
θ	polar angle measured from bottom (lower pole)
$\kappa(\psi)$	dimensionless pressure around sphere [$=2p_a/(\rho V^2)$]
$\mathrm{K}(\psi)$	dimensionless pressure adjusted for distortion around oblate spheroid
Λ	amplitude factor for adjusting pressure drag with $\kappa(\psi)$

Λ', Λ'' amplitude factors for adjusting pressure drag with $K(\psi)$ [lower, upper bound]
ρ density of air
σ surface tension of water in air
Υ amplitude factor for adjusting the drag with $K(\psi)$ [mean forcing]
ϕ angle between tangent in x–z plane and horizontal at upper pole
ψ angle between tangent to drop surface and horizontal at lower pole [$=\pi - \phi$].

REFERENCES

Achenbach, E., 1972: Experiments on the flow past spheres at very high Reynolds numbers. *J. Fluid Mech.*, **54**, 565–575.

Bashforth, F., and J. C. Adams, 1883: *An Attempt to Test the Theories of Capillary Action by Comparing the Theoretical and Measured Forms of Drops of Fluid.* Cambridge University Press, London, 94 pp.

Beard, K. V., 1976: Terminal velocity and shape of cloud and precipitation drops aloft. *J. Atmos. Sci.*, **34**, 851–864.

——, 1977: On the acceleration of large water drops to terminal velocity. *J. Appl. Meteor.*, **16**, 1068–1071.

——, 1982: Raindrop oscillation. *Preprints Conf. on Cloud Physics,* Chicago, Amer. Meteor. Soc., 244–246.

——, 1984: Raindrop oscillations: evaluation of a potential flow model with gravity. *J. Atmos. Sci.*, **41**, 1765–1774.

Blanchard, D. C., 1950: The behavior of water drops at terminal velocity in air. *Trans. Amer. Geophys. Union*, **31**, 836–842.

Brook, M., and D. J. Latham, 1968: Fluctuating radar echo: modulation by vibrating drops. *J. Geophys. Res.*, **73**, 7137–7144.

Caylor, I. J., and A. J. Illingworth, 1986: Observations of the growth and evolution of raindrops using dual-polarization radar. *Preprints 23rd Conf. Radar Meteor.*, Amer. Meteor. Soc., 88–91.

Chandrasekhar, V., V. N. Bringi and J. Vivekanandan, 1984: Estimation of raindrop axial ratios using orthogonally mounted 2D PMS precipitation probes during Maypole. *Preprints 22nd Conf. Radar Meteor.*, Amer. Meteor. Soc., 322–326.

Clift, R., J. R. Grace and M. E. Weber, 1978: *Bubbles, Drops and Particles.* Academic Press, New York, 380 pp.

Cooper, W. A., V. N. Bringi, V. Chandrasekhar and T. A. Seliga, 1983: Analysis of raindrop parameters using a 2D precipitation probe with application to differential reflectivity. *Preprints 21st Conf. Radar Meteorology,* Amer. Meteor. Soc., 448–493.

Cotton, W. R., and N. R. Gokhale, 1967: Collision, coalescence, and breakup of large water drops in a vertical wind tunnel. *J. Geophys. Res.*, **72**, 4041–4049.

Fage, A., 1937: Experiments on a sphere at critical Reynolds Numbers. Aero. Res. Comm., England, Rep. and Memo. No. 1766, 20 pp.

Flachsbart, O., 1927: Untersuchugen uber den Luftwiderstand von Kugeln. *Phys. Z.*, **28**, 461–469.

Foote, G. B., 1969: On the internal circulation of shape of large raindrops. *J. Atmos. Sci.*, **26**, 179–181.

——, 1973: A numerical method for studying liquid drop behavior. *J. Comput. Phys.*, **11**, 507–530.

Forsythe, G. E., M. A. Malcolm and C. B. Moler, 1977: *Computer Methods for Mathematical Computations,* Prentice-Hall, Englewood Cliffs, N.J., 259 pp.

Garner, F. H., and J. J. Lane, 1959: Mass transfer to drops of liquid suspended in a gas stream Part II: Experimental work and results. *Trans. Instn. Chem. Engrs.*, **37**, 162–172.

Green, A. W., 1975: An approximation for the shapes of large raindrops. *J. Appl. Meteor.*, **14**, 1578–1583.

Grover, S. N., and K. V. Beard, 1974: A numerical computation of the collision efficiency of raindrops colliding with aerosol particles and cloud drops. *Preprints Conf. on Cloud Physics,* Amer. Meteor. Soc., Tucson, 120–121.

Gunn, R., 1949: Mechanical resonance in freely falling raindrops. *J. Geophys. Res.*, **54**, 383–385.

Happel, J., and H. Brenner, 1965: *Low Reynolds Number Hydrodynamics,* Prentice-Hall, Englewood Cliffs, N.J., 553 pp.

Hartland, S., and R. W. Hartley, 1976: *Axisymmetric Fluid-Liquid Interfaces,* Elsevier, Amsterdam, 782 pp.

Imai, I., 1950: On the velocity of falling raindrops. *Geophys. Mag. Tokyo,* **21**, 244–249.

Koenig, L. R., 1965: Drop freezing through drop breakup. *J. Atmos. Sci.*, **22**, 448–451.

Lane, W. R., and H. L. Green, 1956: The mechanics of drops and bubbles. *Surveys in Mechanics,* G. K. Batchelor and R. M. Davies (Editors), Cambridge Univ. Press, London, 475 pp. (pp. 183–184).

LeClair, B. P., A. E. Hamielec and H. R. Pruppacher, 1970: A numerical study of the drag on a sphere at low and intermediate Reynolds number. *J. Atmos. Sci.*, **27**, 308–315.

——, ——, —— and W. D. Hall, 1972: A theoretical and experimental study of the internal circulation in water drops falling at terminal velocity in air. *J. Atmos. Sci.*, **29**, 728–740.

Lenard, P., 1904: Uber regen. *Meteor. Z.*, **21**, 248–262 [for English translation see: *Quart. J. Roy. Meteor. Soc.*, **31**, 31, 62–73 (1905).]

McDonald, J. E., 1954a: The shape and aerodynamics of large raindrops. *J. Meteor.*, **11**, 478–494.

——, 1954b: The shape of raindrops. *Sci. Amer.*, **190**, 64–68.

Magono, C., 1954: On the shape of water drops falling in stagnant air. *J. Meteor.*, **11**, 77–79.

Maxworthy, T., 1969: Experiments on the flow around a sphere at high Reynolds numbers. *J. Appl. Mech., Trans. A.S.M.E.*, **36**, 598–607.

Musgrove, C., and M. Brook: Microwave echo fluctuations produced by vibrating water drops. *J. Atmos. Sci.*, **32**, 2001–2007.

Nelson, A. R., and N. R. Gokhale, 1972: Oscillation frequencies of freely suspended water drops. *J. Geophys. Res.*, **77**, 2724–2727.

Oguchi, T., 1981: Scattering from hydrometers: A survey. *Radio Sci.*, **16**, 691–730.

Olsen, R. L., 1981: Cross polarization during precipitation on terrestrial links: A review. *Radio Sci.*, **16**, 761–770.

Pruppacher, H. R., and K. V. Beard, 1970: A wind tunnel investigation of the internal circulation and shape of water drops falling at terminal velocity in air. *Q. J. Roy. Meteor. Soc.*, **96**, 247–256.

——, and J. D. Klett, 1978: *Microphysics of Clouds and Precipitation.* Reidel, Boston, 714 pp.

——, and R. L. Pitter, 1971: A semi-empirical determination of the shape of cloud and rain drops. *J. Atmos. Sci.*, **28**, 86–94.

Rasmussen, R., C. Walcek, H. R. Pruppacher, S. K. Mitra, J. Lew, V. Levizzani, P. K. Wang and U. Barth, 1985: A wind tunnel investigation of the effect of an external electric field on the shape of electrically uncharged rain drops. *J. Atmos. Sci.*, **42**, 1647–1652.

Richards, C. N., and G. A. Dawson, 1971: The hydrodynamic instability of water drops falling at terminal velocity in vertical electric fields. *J. Geophys. Res.*, **76**, 3445–3455.

Reinhart, A., 1964: Das Verhalten fallender Tropfen. *Chemie-Ing.-Technol.*, **36**, 740–746.

Rogers, R. R., 1984: A review of multiparameter radar observations of precipitation. *Radio Sci.*, **19**, 23–26.

Sachidananda, M., and D. S. Zrnić, 1986: A comparison of rain rate estimates from differential propagation phase shift, differential reflectivity and Z–R relationships. Preprints 23rd Conf. Radar Meteorology, Amer. Meteor. Soc., 129–132.

Savic, P., 1953: Circulation and distortion of liquid drops falling through a viscous medium. Natl. Res. Council, Canada, Rep. NRC-MT-22, 50 pp.

Spengler, J. D., and N. R. Gokhale, 1973: Drop impactions. *J. Appl. Meteor.*, **12**, 316–321.

Spilhaus, A. F., 1948: Raindrop size, shape, and falling speed. *J. Meteor.*, **5**, 108–110.